Biodistribution, Dosimetry, and Pharmacokinetics of ^{68}Ga-CBP8: A Type I Collagen–Targeted PET Probe

David Izquierdo-Garcia[1–4], Pauline Désogère[1,5], Mariane Le Fur[1,2,5], Sergey Shuvaev[1,2,5], Iris Y. Zhou[1,2,5], Ian Ramsay[1], Michael Lanuti[2,6], Onofrio A. Catalano[1,2], Ciprian Catana[1,2,5], Peter Caravan[1,2,5], and Sydney B. Montesi[2,5,7]

[1]*Athinoula A. Martinos Center for Biomedical Imaging, Department of Radiology, Massachusetts General Hospital, Boston, Massachusetts;* [2]*Harvard Medical School, Boston, Massachusetts;* [3]*Harvard–MIT Division of Health Sciences and Technology, Cambridge, Massachusetts;* [4]*Bioengineering Department, Universidad Carlos III de Madrid, Spain;* [5]*Institute for Innovation in Imaging, Massachusetts General Hospital, Boston, Massachusetts;* [6]*Division of Thoracic Surgery, Massachusetts General Hospital, Boston, Massachusetts; and* [7]*Division of Pulmonary and Critical Care Medicine, Massachusetts General Hospital, Boston, Massachusetts*

The ^{68}Ga-Collagen Binding Probe #8, ^{68}Ga-CBP8, is a peptide-based, type I collagen–targeted probe developed for imaging of tissue fibrosis. The aim of this study was to determine the biodistribution, dosimetry, and pharmacokinetics of ^{68}Ga-CBP8 in healthy human subjects. **Methods:** Nine healthy volunteers (5 male and 4 female) underwent whole-body ^{68}Ga-CBP8 PET/MRI using a Biograph mMR scanner. The subjects were imaged continuously for up to 2 h after injection of ^{68}Ga-CBP8. A subset of subjects underwent an additional imaging session 2–3 h after probe injection. OLINDA/EXM software was used to calculate absorbed organ and effective dose estimates based on up to 17 regions of interest (16 for men) defined on T2-weighted MR images and copied to the PET images, assuming a uniform distribution of probe concentration in each region. Serial blood sampling up to 90 min after probe injection was performed to assess blood clearance and metabolic stability. **Results:** The mean injected activity (±SD) of ^{68}Ga-CBP8 was 220 ± 100 MBq (range, 113–434 MBq). No adverse effects related to probe administration were detected. ^{68}Ga-CBP8 demonstrated an extracellular distribution with predominantly rapid renal clearance. Doses on the urinary bladder were 0.15 versus 0.19 mGy/MBq for men versus women. The highest absorbed doses for the rest of the organs were measured in the kidneys (0.078 vs. 0.088 mGy/MBq) and the liver (0.032 vs. 0.041 mGy/MBq). The mean effective dose was 0.018 ± 0.0026 mSv/MBq using a 1-h voiding model. The ^{68}Ga-CBP8 signal in the blood demonstrated biexponential pharmacokinetics with an initial distribution half-life of 4.9 min (95% CI, 2.4–9.4 min) and a 72-min elimination half-life (95% CI, 47–130 min). The only metabolite observed had a long blood plasma half-life, suggesting protein-bound ^{68}Ga. **Conclusion:** ^{68}Ga-CBP8 displays favorable in-human characteristics and dosimetry similar to that of other gallium-based probes. ^{68}Ga-CBP8 could therefore be used for noninvasive collagen imaging across a range of human fibrotic diseases.

Key Words: ^{68}Ga-CBP8; PET; fibrosis; collagen; dosimetry

J Nucl Med 2023; 64:775–781
DOI: 10.2967/jnumed.122.264530

Organ fibrosis is a major cause of morbidity and mortality. Fibrotic diseases, such as cirrhosis, pulmonary fibrosis, and systemic sclerosis, or diseases with a fibroproliferative component, such as atherosclerosis, account for nearly half of all human deaths in the United States (*1*). Despite the high burden of fibrotic diseases, limitations exist regarding diagnosis and prognostication (*2*). For many types of fibrosis, diagnosis hinges on histopathology. However, biopsy carries risks and may be impractical for certain fibrotic diseases. Prognostication can be particularly challenging. Disease progression can be heterogeneous, and current imaging modalities such as CT or ultrasound are limited in their ability to determine fibrotic disease activity unless performed serially. In addition, the development of effective antifibrotic therapies has been hampered by difficulties in determining response to therapy and lack of validated noninvasive surrogate markers of early treatment response (*3*).

Several probes have been developed to assess processes driving or associated with tissue fibrosis (*4,5*). Because the mechanistic pathways causing fibrogenesis are similar across organ systems, a molecular probe developed for a specific indication, such as pulmonary fibrosis, may be broadly applicable to other diseases. Noninvasive molecular characterization of fibrosis may offer many advantages over traditional imaging approaches in terms of assessing disease activity, performing molecular phenotyping, and determining treatment response (*6*). Such technology may also be used for drug development to assist with confirming target engagement and assessing drug effect.

Fibrosis is characterized by the excessive deposition of collagen (*7*). We recently developed a type I collagen-targeted PET probe, ^{68}Ga-Collagen Binding Probe #8 (^{68}Ga-CBP8), and performed the first noninvasive collagen visualization in patients with idiopathic pulmonary fibrosis (*8,9*). ^{68}Ga-CBP8 is a peptide-based PET probe that was found to bind to type I collagen with high specificity (*8*). The ^{68}Ga-CBP8 lung signal strongly correlated with the amount of hydroxyproline, as a measure of collagen content, in 2 animal models of lung fibrosis. In addition, this probe was sensitive to detecting treatment response to an antifibrotic therapy. In humans, this probe detected increased collagen in the lungs of those with idiopathic pulmonary fibrosis compared with healthy volunteers (*9*).

The promising results enabled by ^{68}Ga-CBP8 require a more in-depth characterization of the probe properties, including biodistribution, clearance, and dosimetry, for further clinical translation. Here, we present the whole-body distribution, dosimetry estimates, pharmacokinetics, and metabolism of ^{68}Ga-CBP8 in healthy subjects.

MATERIALS AND METHODS

Subject Recruitment and Safety Monitoring

This study was approved by the Mass General Brigham (formerly Partners) Institutional Review Board (protocol 2017P002718) and

Received Jun. 15, 2022; revision accepted Nov. 29, 2022.
For correspondence or reprints, contact David Izquierdo-Garcia (dizquierdogarcia@mgh.harvard.edu) and Sydney Montesi (sbmontesi@partners.org).
Published online Dec. 8, 2022.

registered at clinicaltrials.gov (NCT03535545). All subjects provided written informed consent. Nine healthy subjects (5 men and 4 women) with a median age of 59 y (range, 23–76 y) were included. The subject characteristics are further summarized in Supplemental Table 1 (supplemental materials are available at http://jnm.snmjournals.org). The subjects were closely monitored for safety. Assessment for adverse effects of ^{68}Ga-CBP8 administration included monitoring of vital signs throughout the imaging session and a phone call the day after by a study physician. In addition, the first 6 subjects had electrocardiograms performed before probe injection and after completion of the imaging session.

Synthesis of ^{68}Ga-CBP8

^{68}Ga-CBP8 was manufactured under current good manufacturing practices at the Athinoula A. Martinos Center for Biomedical Imaging radiopharmacy. Two commercially available clinical-grade ^{68}Ge/^{68}Ga generators were used to produce ^{68}Ga-CBP8: the Isotope Technologies Garching generator and the Galli Eo (IRE Elit) generator. Further details about the synthesis of ^{68}Ga-CBP8 can be found in the supplemental materials.

PET/MRI Data Acquisition

Simultaneous PET and MRI (3-tesla) data were acquired using a Biograph mMR scanner (Siemens Healthineers). PET emission data were acquired for approximately 2 h from the start of the injection of ^{68}Ga-CBP8 using 5 bed positions of 240 s each. This allowed the acquisition of 5 time points (frames) per bed position starting around 0, 20, 40, 60, and 85 min after injection (supplemental materials).

PET images were reconstructed in 3-dimensional mode using the standard reconstruction parameters provided by the manufacturer, that is, ordinary Poisson ordered-subset expectation maximization with 3 iterations and 21 subsets with a postreconstruction isotropic gaussian filter of 4 mm with a maximum extended axial coverage (head to mid thigh) of up to 1 m. Simultaneously with the PET data acquisition, the MRI data were acquired with several sequences, including T2-weighted short-tau inversion recovery half-Fourier acquisition single-shot turbo spin-echo images acquired coronally during 2 concatenated breath holds and a dual-echo Dixon for attenuation correction purposes. The supplemental materials provide further details about the PET/MRI data acquisition.

Dosimetry Analysis

Human dosimetry estimates were calculated using OLINDA software, version 2.2 (OLINDA/EXM), using the International Commission on Radiological Protection 103 standard male and female models (*10*). A uniform distribution of radiotracer concentration throughout the organs was assumed. Regions of interest were drawn at each individual multibed acquisition, as described by Pfeifer et al. (*11*) and Laforest et al. (*12*), on the coronal T2-weighed (half-Fourier single-shot turbo spin-echo) images using OsiriX MD, version 12 (Pixmeo SARL), covering all organs with visible uptake above the background (supplemental materials). Regions of interest were then resliced and propagated into the corresponding PET frames. Mean radiotracer concentrations were obtained per slice, and a weighted average was used to obtain 1 mean concentration value per organ. The average region-of-interest values were then converted into the percentage injected dose (%ID) per organ by normalizing to the total injected activity and using the phantom organ mass scaled by the ratio of the phantom's weight over the patient's actual weight, as shown by Laforest et al. (*12,13*) (supplemental materials). The time-dependent curves of the %ID per organ were then fit using an in-house script (Python, version 3.1) to provide the corresponding estimates of the organ time-integrated activity coefficients by analytic integration of a function using a combination of mono- and biexponentials (Supplemental Table 2) (*12*). The lumbar vertebrae dose was assigned to the red marrow using the weight provided in OLINDA, version 2.2, which follows the European Association of Nuclear Medicine guidelines (*14*). The time-integrated activity coefficient for the urinary bladder was calculated using the voiding model on the OLINDA software in a similar manner, as explained by Sprague et al. (*15*).

Finally, the value assigned for the remainder of the body was calculated as the difference from the total activity at a time point minus the accounted activity in all organs (*11*). Total organ-absorbed doses were calculated for each subject and then averaged together to create both the male and the female phantom estimated doses.

Blood Analyses

Serial venous blood sampling for measurement of ^{68}Ga-CBP8 blood clearance and metabolism was performed on 8 of the 9 subjects using an intravenous catheter placed in the arm opposite the one used for probe injection. Up to 6 samples per subject were collected at around 3, 10, 20, 30, 60, and 90 min after injection. The exact time points were used in data analysis. A 300-μL aliquot of each whole-blood sample was weighed, its radioactivity was measured with a γ-counter (Wizard 2480; PerkinElmer), and the %ID per gram was calculated (the supplemental materials describe γ-counter calibration). Another 2 mL of each blood sample was centrifuged at 4,000*g* for 5 min at 4°C to separate plasma. A 300-μL aliquot of plasma was weighed, and its activity was counted. Whole blood as the %ID per gram and

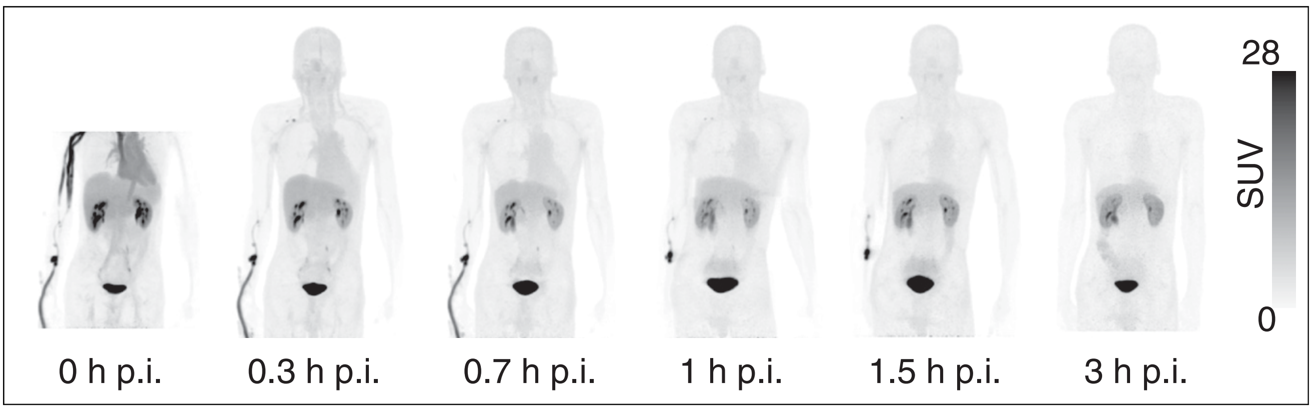

FIGURE 1. Maximum-intensity-projection coronal images of representative subject (subject 4) showing probe uptake pattern of ^{68}Ga-CBP8 from time of injection up to 3 h after injection across all organs. Note fast clearance of tracer from main organs, mostly through renal excretion, and smaller portion through hepatobiliary system, providing desired low, nonspecific background activity across all organs. p.i. = after injection.

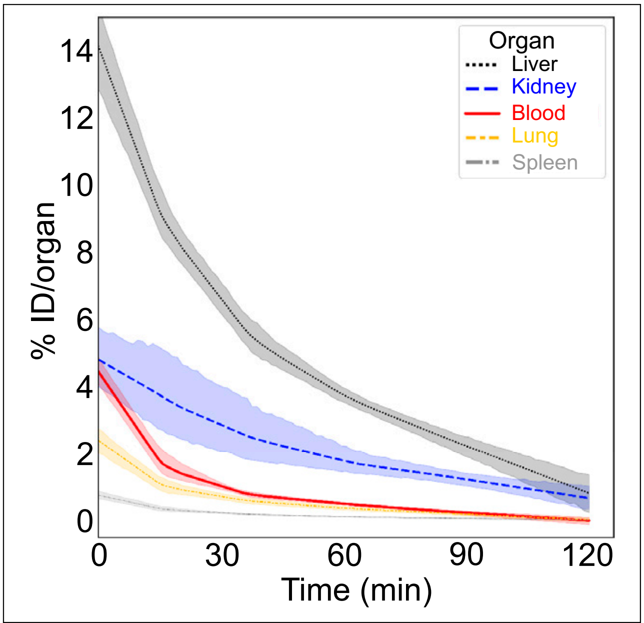

FIGURE 2. Time–activity curves for selected organs representing %ID per organ across time from injection up to 120 min. Each postinjection curve represents average across subjects, with shaded area representing 95% CI of mean.

plasma %ID per gram were plotted as a function of time and fit to a biexponential model:

$$\%\mathrm{ID}/\mathrm{g}(t) = Ae^{-\alpha t} + Be^{-\beta t},$$

where t is time, A and B are the fraction of injected activity for each individual exponential and α and β are the exponential rate constants for each individual exponential function.

Distribution half-life is given as $\ln(2)/\alpha$, and elimination half-life is given as $\ln(2)/\beta$. The supplemental materials show metabolite analysis using analytic high-performance liquid chromatography.

RESULTS

Synthesis

^{68}Ga-CBP8 was initially produced using ^{68}Ga from an Isotope Technologies Garching generator. The formulation of the precursor and the labeling protocol were optimized for this generator (Supplemental Table 3). The precursor was formulated in 3 M sodium acetate buffer (pH 4.5). Such a high buffer concentration was required to reach an optimal labeling pH of 4.0 after adding the $^{68}Ga^{3+}$ radioisotope eluted in 6 mL of 0.05 M HCl. Purification of the labeled product was required to remove radiometal impurities, including any ^{68}Ge, and excess buffer was required to meet quality control specifications. During the study, the U.S. Nuclear Regulatory Commission and the Massachusetts Department of Health issued a requirement that ^{68}Ga generators for human use have a specification of less than 0.001% ^{68}Ge breakthrough. The specification for the Isotope Technologies Garching generator was less than 0.005%, and although the ^{68}Ga-CBP8 process had a purification step to remove any ^{68}Ge, we were required to change to a different generator. When we moved to the Galli Eo generator, radiolabeling with the initial precursor formulation was unsuccessful, with radiochemical purity in the 90%–95% range. The formulation of the precursor was reoptimized and the labeling protocol was adapted for $^{68}GaCl_3$ eluted from the Galli Eo generator in 1.1 mL of 0.1 M HCl. Optimal labeling conditions were found using the CBP8 precursor formulated in 1.5 M sodium acetate at pH 4.0 (Supplemental Table 3). After the labeling reaction, the pH was adjusted to pH 6–8 using a 0.5 M solution of sodium phosphate dibasic, and the solution was diluted to 20 mL with an 80 mM sucrose solution to reach an osmolality suitable for intravenous injection (320–380 mOsm). No further purification was required since the

TABLE 1
SUV_{mean} at 90 min Postinjection for Several Organs Across All Subjects

Region of interest	SUV_{mean} at 90 min			
	All*	Female	Male	P, female vs. male†
Left ventricle	0.96 (0.73–1.28)	1.05 (0.73–1.28)	0.91 (0.73–1.12)	0.65
Myocardium	0.62 (0.27–1.36)	0.65 (0.27–0.86)	0.58 (0.37–1.36)	0.99
Lung	0.31 (0.19–0.47)	0.33 (0.22–0.47)	0.29 (0.19–0.38)	0.79
Skeletal muscle	0.32 (0.29–0.47)	0.31 (0.29–0.47)	0.32 (0.29–0.42)	0.99
Pancreas	1.13 (0.73–1.49)	1.42 (1.23–1.49)	0.89 (0.73–1.44)	0.14
Small intestine	0.85 (0.58–1.54)	0.79 (0.66–0.86)	0.94 (0.58–1.54)	0.39
Large intestine	0.71 (0.34–1.15)	0.58 (0.34–1.15)	0.79 (0.52–0.93)	0.79
Liver	2.44 (1.88–2.97)	2.56 (2.46–2.97)	2.31 (1.88–2.82)	0.14
Kidney	6.98 (5.18–9.32)	8.25 (7.33–9.20)	6.55 (5.18–9.32)	0.25
Uterus	NA	2.01 (1.81–3.47)	NA	NA
Prostate	NA	NA	1.55 (0.04–4.09)	NA
Brain	0.08 (0.03–0.09)	0.06 (0.03–0.09)	0.08 (0.05–0.09)	0.64

*Except subject 7 because of unavailable data around 90 min.
†Wilcoxon rank sum test.
NA = not applicable.
Data are median and range.

TABLE 2
Organ-Absorbed Doses and Effective Doses for Standard Male and Female Phantoms Using International Commission on Radiological Protection 103 Models

Target organ	Organ dose (mGy/MBq)		
	Male	Female	*P**
Adrenals	0.018 (0.0032)	0.019 (0.0025)	0.016
Brain	0.0021 (0.0003)	0.0025 (0.0003)	<0.0001
Breasts	NA	0.011 (0.0022)	N/A
Esophagus	0.0093 (0.0010)	0.011 (0.0012)	<0.0001
Eyes	0.0076 (0.0009)	0.0092 (0.0011)	<0.0001
Gallbladder wall	0.019 (0.0067)	0.021 (0.0078)	<0.0001
Left colon	0.020 (0.0050)	0.022 (0.0047)	<0.0001
Small intestine	0.020 (0.0020)	0.024 (0.0024)	<0.0001
Stomach wall	0.013 (0.0018)	0.015 (0.0020)	<0.0001
Right colon	0.011 (0.0011)	0.013 (0.0014)	<0.0001
Rectum	0.012 (0.0005)	0.018 (0.0006)	<0.0001
Heart wall	0.016 (0.0013)	0.021 (0.0017)	<0.0001
Kidneys	0.078 (0.030)	0.088 (0.034)	<0.0001
Liver	0.032 (0.0036)	0.041 (0.0045)	<0.0001
Lungs	0.0067 (0.0008)	0.0085 (0.0010)	<0.0001
Ovaries	NA	0.014 (0.0007)	NA
Pancreas	0.017 (0.0023)	0.021 (0.0027)	<0.0001
Prostate	0.021 (0.013)	NA	NA
Salivary glands	0.0082 (0.0010)	0.010 (0.0012)	<0.0001
Red marrow	0.010 (0.0006)	0.012 (0.0008)	<0.0001
Osteogenic cells	0.0085 (0.0006)	0.0089 (0.0007)	<0.0001
Spleen	0.013 (0.0020)	0.016 (0.0023)	<0.0001
Testes	0.013 (0.0058)	NA	NA
Thymus	0.0089 (0.0010)	0.011 (0.0012)	<0.0001
Thyroid	0.0085 (0.0010)	0.010 (0.0012)	<0.0001
Urinary bladder wall	0.15 (0.034)	0.19 (0.043)	<0.0001
Uterus	NA	0.029 (0.015)	NA
Total body	0.011 (0.0009)	0.014 (0.0010)	<0.0001
Effective dose (mSv/MBq)	0.016 (0.0008)	0.021 (0.0012)	<0.0001

*Paired *t* test.
NA = not applicable.
Data are mean followed by SD in parentheses.

generator met specifications for ^{68}Ge breakthrough. Using this formulation and labeling protocol, ^{68}Ga-CBP8 was obtained with high radiochemical purity (>95%) and radiochemical yield greater than 80% after sterile filtration.

Safety, Biodistribution, and Dosimetry Estimates

The mean administered activity was 220 ± 100 MBq (range, 113–434 MBq). There were no adverse or clinically detectable pharmacologic effects related to ^{68}Ga-CBP8 in any of the 9 subjects. No significant changes in vital signs or electrocardiograms were observed.

Figure 1 demonstrates a typical biodistribution of ^{68}Ga-CBP8 over time. ^{68}Ga-CBP8 demonstrated rapid renal clearance, with some uptake in the liver and biliary tract and low background uptake in other organs, such as the lungs. Figure 2 shows the time–activity curves for selected organs, including the lungs, liver, kidneys, spleen, and blood pool, demonstrating fast probe clearance and low background activity in healthy regions. Table 1 lists SUV_{mean} at 90 min after injection for various tissues. No differences were observed in SUV_{mean} between men and women. The ^{68}Ga-CBP8 signal in the blood, measured in the left ventricular region of interest, demonstrated biexponential pharmacokinetics with an initial distribution half-life of 4.4 min (95% CI, 3.1–5.8 min) and a 70.4-min elimination half-life (95% CI, 70.2–70.5 min). These values align with estimates of distribution and elimination half-life determined from venous blood sampling. Median fractions and half-lives for the bladder

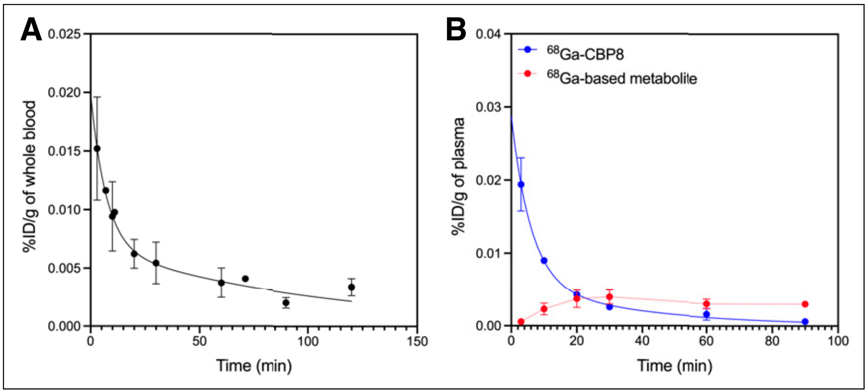

FIGURE 3. (A) Whole-blood clearance of ^{68}Ga-CBP8 in 8 subjects. (B) Blood plasma clearance of intact ^{68}Ga-CBP8 probe and ^{68}Ga-based metabolite observed by high-performance liquid chromatography.

model were 34% (range, 17%–38%) and 29 min (range, 15–47 min), respectively.

The organ-absorbed doses and the estimated effective doses for a 1-h voiding cycle are shown in Table 2. The urinary bladder was the organ with the highest absorbed dose for men and women (0.15 vs. 0.19 mGy/MBq, respectively), followed by the kidneys (0.078 vs. 0.088 mGy/MBq, respectively) and the liver (0.032 vs. 0.041 mGy/MBq, respectively). The mean effective dose was 0.018 ± 0.0026 mSv/MBq (0.016 ± 0.0008 mSv/MBq for men and 0.021 ± 0.0012 mSv/MBq for women). All organs showed higher absorbed doses for women to a significance level of $P < 0.0001$, except for the adrenals ($P = 0.016$). Overall, time-integrated activity coefficients did not show significant differences between men and women (Supplemental Table 4). An example of the data fitting and the square of the Pearson correlation coefficient (r^2) per organ are shown in Supplemental Figure 1 and Supplemental Table 4, respectively.

Pharmacokinetics and Metabolism

Analysis of radioactivity in serial venous blood samples showed a biexponential elimination (Fig. 3A). Fitting the blood radioactivity versus time curves to a biexponential function gave a distribution half-life of 4.9 min (95% CI, 2.4–9.4 min) and an elimination half-life of 72 min (95% CI, 47–130 min), consistent with a probe that has low protein binding, predominantly renal elimination, and an extracellular distribution.

Radio–high-performance liquid chromatography analysis of plasma samples showed that ^{68}Ga-CBP8 is fairly stable with respect to metabolism (Supplemental Fig. 2). A single, small metabolite was observed, and this metabolite had a much longer blood half-life than ^{68}Ga-CBP8 (Fig. 3B). Because ^{68}Ga-CBP8 is rapidly eliminated from the plasma but the metabolite is not, the fraction of intact ^{68}Ga-CBP8 circulating changed as a function of time, with 97.1%, 79.9%, 54.1%, 39.8%, 22.9%, and 17.3% of the circulating dose corresponding to the intact probe at 3, 10, 20, 30, 60, and 90 min, respectively, after injection of the probe (Fig. 3B). On the basis of the long plasma half-life of the metabolite, we speculate that this may be due to the transmetalation of ^{68}Ga to a plasma protein.

DISCUSSION

Here we present the first-in-humans dosimetry and pharmacokinetic results of ^{68}Ga-CBP8. Our study has several notable findings. In a small group of healthy volunteers, there were no adverse events deemed related to ^{68}Ga-CBP8. ^{68}Ga-CBP8 had an extracellular distribution, displayed good metabolic stability, and was rapidly cleared from the circulation, with a distribution half-life of about 5 min and an elimination half-life of about 70 min. Doses were higher in women than men, similar to other dosimetry studies (*13,16–19*). However, neither the probe uptake (SUV_{mean} at 90 min; Table 1) nor the time-integrated activity coefficients (Supplemental Table 4) showed significant sex differences, suggesting that the higher S values per organ on the female phantom, as a result of the smaller female organ and body sizes (*19*), are responsible for the observed doses differences. ^{68}Ga-CBP8 displays dosimetry values

TABLE 3
Comparison of ^{68}Ga-CBP8 with Mean Effective Doses of Other ^{68}Ga-Based PET Probes and ^{18}F-FDG

Compound	Effective dose (mSv/MBq)	Voiding model	Reference
^{68}Ga-NODAGA-RGByK	0.016–0.024	30 min and 1 h	(*16*)
^{68}Ga-NODAGA-MJ9	0.018–0.023	30 min and 1 h	(*17*)
^{68}Ga-P16–093	0.022–0.027	55 min (single)	(*18*)
^{68}Ga-DOTA-E-[c(RGDfK)]2	0.017–0.024	1 h	(*19*)
^{68}Ga-DOTATATE	0.021	Urine collection	(*20*)
^{68}Ga-DOTATOC	0.021	Urine collection	(*20*)
^{68}Ga-FAPI-2	0.018	Unspecified	(*21*)
^{68}Ga-FAPI-4	0.016	Unspecified	(*21*)
^{68}Ga-FAPI-74	0.016	Unspecified	(*22*)
^{18}F-FDG	0.020 (0.013–0.029)	Unspecified	(*23*)
^{68}Ga-CBP8	0.018	1 h	This study

Effective doses are mean and/or range.

similar to those of other state-of-the-art ^{68}Ga-based tracers, including other NODAGA-based probes (Table 3) (*16–22*). In addition, the mean effective dose of 0.018 mSv/MBq with ^{68}Ga-CBP8 is in line with the standard and widely used ^{18}F-FDG, with mean effective doses of about 0.02 mSv/MBq (range, 0.013–0.029 mSv/MBq) (*23*). The mean effective dose was higher in women than men (0.021 vs. 0.016 mSv/MBq) because of the higher absorbed dose in the uterus and ovaries than in the testes and prostate.

There is increasing development and application of molecular probes for detection of fibrosis (*24,25*). Collagen is a particularly attractive target because it is the most abundant of proteins in the fibrotic extracellular matrix (*26*). ^{68}Ga-CBP8 is the first collagen-specific PET probe that has been translated into humans for fibrosis imaging. ^{68}Ga-CBP8 is a peptide-based probe that binds type I collagen with high specificity and a dissociation constant of $2.1 \pm 0.1\ \mu M$ for human collagen (*8*). Ex vivo correlation of the %ID and lung collagen was strong in both bleomycin-injured mice and explanted lungs from patients with pulmonary fibrosis. In humans, ^{68}Ga-CBP8 uptake was increased in the whole lungs of subjects with idiopathic pulmonary fibrosis compared with healthy volunteers (0.65 vs. 0.48 SUV_{mean} at 60 min) (*9*). However, the PET signal in the lungs of subjects with pulmonary fibrosis is notably heterogeneous, with SUV_{mean} greater than 2 in areas of high ^{68}Ga-CBP8 uptake, presumably indicative of active fibrosis. In the healthy volunteers in this study, there was a reduced background signal (<1 SUV_{mean} at 90 min) for most organs, suggesting that this probe is likely to be useful for the detection of active fibrosis across multiple organ systems. ^{68}Ga-CBP8 has several advantages over other clinically used approaches to fibrosis detection. ^{68}Ga-CBP8 enables noninvasive collagen detection, thus obviating the risks associated with biopsy for histopathologic characterization. Imaging modalities such as CT or ultrasound can detect structural changes resulting from tissue fibrosis but have a limited ability to assess fibrotic disease activity at any one time point.

Our results expand on prior experience with ^{68}Ga-CBP8 by demonstrating favorable pharmacokinetic parameters and dosimetry estimates in humans. In healthy volunteers, ^{68}Ga-CBP8 had an extracellular distribution, fast clearance, and metabolic stability. Murine studies with ^{64}Cu-CBP7, a probe similar to ^{68}Ga-CBP8, also demonstrated fast clearance (blood half-life of 20 min in mice) and metabolic stability, with more than 80% of the probe still intact at 120 min (*27*).

Our results have several implications for broader clinical translation of ^{68}Ga-CBP8. First, we found that the synthesis of ^{68}Ga-CBP8 needed to be adapted to the type of generator used because of generator-dependent changes in yield and purity. Next, because of the rapid clearance, image acquisition can occur within a short time from probe injection. In healthy individuals, ^{68}Ga-CBP8 displayed low background uptake in all organs other than the urinary tract, liver, and biliary tree. Thus, ^{68}Ga-CBP8 may be applied to detect excess collagen in multiple organ systems. The favorable dosimetry estimates lessen the risks of repeated ^{68}Ga-CBP8 PET for detection of fibrosis progression and response to treatment.

Our study has several limitations. First, the increased bladder uptake induced large partial-volume effects on neighboring tissues. These partial-volume effects largely affected measurements of the ovaries. To avoid biasing the dosimetry estimates, we did not include the ovaries' measured uptake in the dosimetry calculations in OLINDA; instead, they were considered part of the remainder of the body region. However, increased uptake in the ovaries is not anticipated for younger healthy volunteers (our female cohort's average age was <40 y); thus, its inclusion as part of the remainder of the body remains valid. Lastly, we used a simultaneous PET/MRI scanner to obtain our PET images. Although the use of PET/MRI compared with PET/CT eliminates the extra ionizing radiation from the CT component, the use of MRI-based techniques for attenuation correction on the whole-body level is still not ideal (*28*). Despite these limitations, our results are highly encouraging, demonstrating low organ doses and low mean effective doses and further supporting the clinical application of this probe to fibrotic diseases.

CONCLUSION

^{68}Ga-CBP8 demonstrates an extracellular distribution, rapid renal clearance, and metabolic stability in the blood. Dosimetry estimates are similar to those of other gallium-based probes. Thus, ^{68}Ga-CBP8 is a promising probe for imaging of collagen and tissue fibrosis.

DISCLOSURE

This work was supported by grants from the National Heart Lung and Blood Institute (R01HL116315, R01HL131907, R01HL153606, K23HL150331, and K25HL148837) and the National Institutes of Health (NIH) Office of the Director (S10OD028499). Peter Caravan and Pauline Désogère are inventors on U.S. patent US10,471,162, which covers ^{68}Ga-CBP8. David Izquierdo-Garcia has received consulting fees from Collagen Medical LLC. Michael Lanuti receives consulting fees from BMS, AstraZeneca, and Iovance. Peter Caravan holds equity in and receives consulting income from Collagen Medical LLC, holds equity in Reveal Pharmaceuticals, and has research funding from Takeda, Pliant Therapeutics, and Janssen. Sydney Montesi was supported by the NIH (K23HL15033), the Francis Family Foundation, and the National Scleroderma Foundation during the conduct of this study. She has received funding through her institution from Merck, United Therapeutics, Boehringer Ingelheim, and Pliant Therapeutics. She has also received funding from the American Thoracic Society and Three Lakes Foundation. She has received consulting fees from DevPro Biopharma, Gilead Sciences, and Roche; advisory board fees from APIE Therapeutics; and royalties from Wolters Kluwer. No other potential conflict of interest relevant to this article was reported.

ACKNOWLEDGMENTS

We thank the Athinoula A. Martinos Center for Biomedical Imaging PET/MRI core, Grae Arabasz, Shirley Hsu, Regan Butterfield, Oliver Ramsay, Matthew Drummond, Samantha Zygmont, Dr. Leo Ginns, Layla Rahimi, Staci Mangini, and Demi Ajao for their assistance.

KEY POINTS

QUESTION: What are the dosimetry and kinetic characteristics of the collagen-targeted probe ^{68}Ga-CBP8 in healthy volunteers?

PERTINENT FINDINGS: ^{68}Ga-CBP8 displays favorable kinetics with an extracellular distribution, fast renal clearance, and metabolic stability. Effective doses are similar to those reported for other gallium tracers.

IMPLICATIONS FOR PATIENT CARE: ^{68}Ga-CBP8 is a promising probe for noninvasive imaging of collagen that might be applied to a range of fibrotic diseases.

REFERENCES

1. Wynn TA. Fibrotic disease and the TH1/TH2 paradigm. *Nat Rev Immunol.* 2004;4: 583–594.
2. Spagnolo P, Ryerson CJ, Putman R, et al. Early diagnosis of fibrotic interstitial lung disease: challenges and opportunities. *Lancet Respir Med.* 2021;9:1065–1076.
3. White ES, Thomas M, Stowasser S, Tetzlaff K. Challenges for clinical drug development in pulmonary fibrosis. *Front Pharmacol.* 2022;13:823085.
4. Klinkhammer BM, Lammers T, Mottaghy FM, Kiessling F, Floege J, Boor P. Non-invasive molecular imaging of kidney diseases. *Nat Rev Nephrol.* 2021;17:688–703.
5. Désogère P, Montesi SB, Caravan P. Molecular probes for imaging fibrosis and fibrogenesis. *Chemistry.* 2019;25:1128–1141.
6. Montesi SB, Désogère P, Fuchs BC, Caravan P. Molecular imaging of fibrosis: recent advances and future directions. *J Clin Invest.* 2019;129:24–33.
7. Wynn TA. Cellular and molecular mechanisms of fibrosis. *J Pathol.* 2008;214: 199–210.
8. Désogère P, Tapias LF, Hariri LP, et al. Type I collagen–targeted PET probe for pulmonary fibrosis detection and staging in preclinical models. *Sci Transl Med.* 2017;9:eaaf4696.
9. Montesi SB, Izquierdo-Garcia D, Désogère P, et al. Type I collagen–targeted positron emission tomography imaging in idiopathic pulmonary fibrosis: first-in-human studies. *Am J Respir Crit Care Med.* 2019;200:258–261.
10. Stabin MG, Siegel JA. RADAR dose estimate report: a compendium of radiopharmaceutical dose estimates based on OLINDA/EXM version 2.0. *J Nucl Med.* 2018; 59:154–160.
11. Pfeifer A, Knigge U, Mortensen J, et al. Clinical PET of neuroendocrine tumors using ^{64}Cu-DOTATATE: first-in-humans study. *J Nucl Med.* 2012;53:1207–1215.
12. Laforest R, Dehdashti F, Lewis JS, Schwarz SW. Dosimetry of $^{60/61/62/64}$Cu-ATSM: a hypoxia imaging agent for PET. *Eur J Nucl Med Mol Imaging.* 2005;32:764–770.
13. Laforest R, Ghai A, Fraum TJ, et al. First-in-human evaluation of safety and dosimetry of ^{64}Cu-LLP2A for PET imaging. *J Nucl Med.* 2022;64:320–328.
14. Hindorf C, Glatting G, Chiesa C, Lindén O, Flux G. EANM dosimetry committee guidelines for bone marrow and whole-body dosimetry. *Eur J Nucl Med Mol Imaging.* 2010;37:1238–1250.
15. Sprague DR, Chin FT, Liow JS, et al. Human biodistribution and radiation dosimetry of the tachykinin NK1 antagonist radioligand [^{18}F]SPA-RQ: comparison of thin-slice, bisected, and 2-dimensional planar image analysis. *J Nucl Med.* 2007;48:100–107.
16. Gnesin S, Mitsakis P, Cicone F, et al. First in-human radiation dosimetry of ^{68}Ga-NODAGA-RGDyK. *EJNMMI Res.* 2017;7:43.
17. Gnesin S, Cicone F, Mitsakis P, et al. First in-human radiation dosimetry of the gastrin-releasing peptide (GRP) receptor antagonist ^{68}Ga-NODAGA-MJ9. *EJNMMI Res.* 2018;8:108.
18. Green MA, Hutchins GD, Bahler CD, et al. [^{68}Ga]Ga-P16-093 as a PSMA-targeted PET radiopharmaceutical for detection of cancer: initial evaluation and comparison with [^{68}Ga]Ga-PSMA-11 in prostate cancer patients presenting with biochemical recurrence. *Mol Imaging Biol.* 2020;22:752–763.
19. López-Rodríguez V, Galindo-Sarco C, García-Pérez FO, Ferro-Flores G, Arrieta O, Ávila-Rodríguez MA. PET-based human dosimetry of the dimeric $\alpha_v\beta_3$ integrin ligand ^{68}Ga-DOTA-E-[c(RGDfK)] 2, a potential tracer for imaging tumor angiogenesis. *J Nucl Med.* 2016;57:404–409.
20. Sandström M, Velikyan I, Garske-Román U, et al. Comparative biodistribution and radiation dosimetry of ^{68}Ga-DOTATOC and ^{68}Ga-DOTATATE in patients with neuroendocrine tumors. *J Nucl Med.* 2013;54:1755–1759.
21. Giesel FL, Kratochwil C, Lindner T, et al. ^{68}Ga-FAPI PET/CT: biodistribution and preliminary dosimetry estimate of 2 DOTA-containing FAP-targeting agents in patients with various cancers. *J Nucl Med.* 2019;60:386–392.
22. Giesel FL, Adeberg S, Syed M, et al. FAPI-74 PET/CT using either ^{18}F-AlF or cold-kit ^{68}Ga labeling: biodistribution, radiation dosimetry, and tumor delineation in lung cancer patients. *J Nucl Med.* 2021;62:201–207.
23. Quinn B, Dauer Z, Pandit-Taskar N, Schoder H, Dauer LT. Radiation dosimetry of ^{18}F-FDG PET/CT: incorporating exam-specific parameters in dose estimates. *BMC Med Imaging.* 2016;16:41.
24. Brody SL, Gunsten SP, Luehmann HP, et al. Chemokine receptor 2–targeted molecular imaging in pulmonary fibrosis: a clinical trial. *Am J Respir Crit Care Med.* 2021;203:78–89.
25. Lukey PT, Coello C, Gunn R, et al. Clinical quantification of the integrin αvβ6 by [^{18}F]FB-A20FMDV2 positron emission tomography in healthy and fibrotic human lung (PETAL study). *Eur J Nucl Med Mol Imaging.* 2020;47:967–979.
26. Frantz C, Stewart KM, Weaver VM. The extracellular matrix at a glance. *J Cell Sci.* 2010;123:4195–4200.
27. Désogère P, Tapias LF, Rietz TA, et al. Optimization of a collagen-targeted PET probe for molecular imaging of pulmonary fibrosis. *J Nucl Med.* 2017;58:1991–1996.
28. Keller SH, Holm S, Hansen AE, et al. Image artifacts from MR-based attenuation correction in clinical, whole-body PET/MRI. *MAGMA.* 2013;26:173–181.